ADVANCED FUNCTIONAL MATERIALS
www.afm-journal.de

All 3D-Printed Soft High-Density Surface Electromyography Electrode Arrays for Accurate Muscle Activation Mapping and Decomposition

Yi Zhao, Chen Chen, Baoyang Lu, Xiangyang Zhu, and Guoying Gu**

High-density surface electromyography (sEMG) electrode arrays enable the recording of tens to hundreds of channels of electromyographic signals, which have found wide applications in clinics and human-machine interfaces. However, current manufacturing technologies of high-density sEMG electrode arrays generally involve high-cost equipments, complicated procedures, and insufficient programmability, severely hampering the rational design and practical applications of customized yet cost-effective high-density electrode arrays. Herein, the facile and efficient fabrication of novel 32-channel soft high-density sEMG electrode arrays by an all-printed technique based on multimaterial direct ink writing 3D printing is presented. By employing rational four-layer stacked structure designs with systematic ink printability evaluation, it can successfully realize seamless interfacial integration during the multimaterial printing, achieving reproducible, programmable, continuous fabrication of soft high-density sEMG electrode arrays. The all 3D-printed soft electrode arrays exhibit excellent stability, low impedance, and high signal-to-noise ratio superior to commercial products with an increase of 32.2%. Such intriguing properties enable this all 3D-printed electrode arrays the unique capability of mapping muscle activation of the forearm, and the motor unit action potential trains can be precisely identified for varying hand gestures to effectively explore the innovative human-machine interface toward diverse applications such as teleoperation and prosthetic control.

1. Introduction

Surface electromyography (sEMG) signals, the electric manifestation of muscle activations recorded from the skin surface and containing rich α motor nerve information,[1] have been widely utilized in clinical diagnostics and human-machine interfaces, such as hand function rehabilitation of stroke patients[2,3] and prosthetic control,[4–6] etc. As the most important non-invasive recording tools of sEMG signals, high-density sEMG electrode arrays[7,8] can realize long-term, continuous monitoring of multi-channel signals on the skin without penetrating the muscles. However, existing high-density electrode arrays, generally made by coating metals (e.g., Ag/AgCl, Ag, Cu, Au) on plastics (e.g., PI, PET) accompanied with a series of lithography, etching, and subtractive manufacturing, display insufficient softness, inferior conformability with human skin, poor customization, and non-programmable manufacturing,[9] resulting in inaccurate signal acquisition and high cost yet unsatisfactory customer experience. While intensive efforts have been devoted to address these obstacles, the rational design and integrated fabrication of intrinsically soft high-density sEMG electrode arrays with reliable performance and stability for accurate signal recording, muscle activation mapping and decomposition, still remain a grand but ongoing challenge.

Typical high-density sEMG electrode arrays are designed as an integrated sandwich structure with a total thickness of several hundred micrometers consisting of the substrate layer, the electrode layer, and the encapsulation layer.[10–12] Their integrated manufacturing process usually involves complex procedures like spin coating of dielectric materials to form the substrate layer,[13–15,20,21,26] printing[16–20,27]/etching[14,26]/masking[21,22]/vacuum sputtering[15,25,26] to fabricate the electrode channel, and final encapsulation by laser cutting of preformed insulation films[16,17,19,20,23–25] and transfer printing by manual alignment.[19,23,24,26] Inevitably, such process induces high cost on equipments, complicated procedures, as well as insufficient

Y. Zhao, C. Chen, X. Zhu, G. Gu
Robotics Institute and State Key Laboratory of Mechanical System and Vibration
School of Mechanical Engineering
Shanghai Jiao Tong University
Shanghai 200240, China
E-mail: mexyzhu@sjtu.edu.cn; guguoying@sjtu.edu.cn
Y. Zhao, C. Chen, X. Zhu, G. Gu
Meta Robotics Institute
Shanghai Jiao Tong University
Shanghai 200240, China
B. Lu
Jiangxi Key Laboratory of Flexible Electronics
Flexible Electronics Innovation Institute
Jiangxi Science and Technology Normal University
Nanchang 330013, China

The ORCID identification number(s) for the author(s) of this article can be found under https://doi.org/10.1002/adfm.202312480

DOI: 10.1002/adfm.202312480

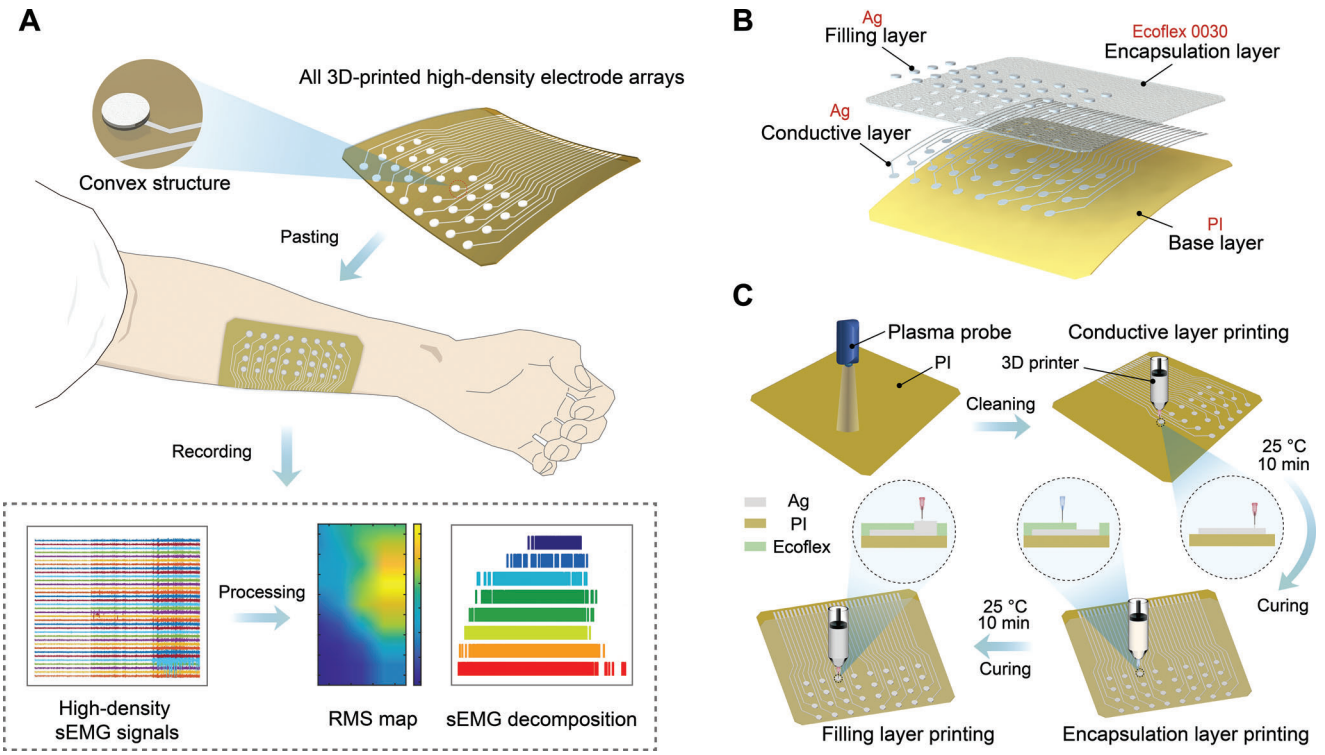

Figure 1. All 3D-printed soft high-density electrode arrays. A) Schematic illustration of all 3D-printed soft electrode arrays pasted on the forearm to realize accurate sEMG recording. B) Structure design of the all-printed high-density electrode arrays. The electrode arrays consist of a four-layer stacked structure. The material of each layer is marked in red font. C) All 3D-printing process of the high-density sEMG electrode arrays. After plasma cleaning of the substrate, the electrode arrays are printed in three sequential steps with multimaterial printing nozzles.

programmability. As a low-cost, programmable, and flexible printing technique, direct ink writing (DIW) 3D printing can be potentially utilized to achieve customized, continuous integrated manufacturing of high-density electrode arrays.[27–30] However, realizing integrated 3D printing of soft, reliable high-density electrode arrays still faces some technical limitations from high-performance yet stable material choices, coordination of multimaterial inks with differential viscoelasticity to achieve diverse electrode structures, shape fidelity control, and finally to tricky interfacial integration.

In this work, we demonstrate a novel all 3D-printed process to manufacture customized thin-film, soft electrode arrays for continuous monitoring of high-density sEMG signals (**Figure** 1A). The electrode arrays consist of a four-layer stacked structure with 32 channels in a 4 × 8 arrangement. In addition to the base layer, all materials are printed by DIW printer layer by layer without any other processing strategy. To achieve such multimaterial printing, we first characterize printing parameters for two materials with significant differences in viscoelasticity, i.e., soft elastic Ag ink and Ecoflex 0030 silicone rubber ink. Based on the printability evaluation, optimal printing parameters and patterns are designed for different functional layers to eliminate diffusion effects to gain high shape fidelity and seamless interfacial integration. Subsequently, the structures containing the polyline, the hollow plane, and the convex cylinder are printed in sequence to achieve accurate interface integration of multimaterials and continuous manufacturing of customized soft high-density electrode arrays with the proposed all-printed process. The electrical properties of printed electrodes demonstrate relatively low skin-electrode impedance, resulting in a 32.2% enhancement of signal-to-noise ratio (SNR) under 30% maximum voluntary contraction (MVC) superior to the commercial products. By applying the electrode array to the forearm, changing contraction centroids of flexor digitorum superficials (FDS) muscle for different finger flexions can be clearly observed through the heat maps, showing the high spatial resolution of the 3D-printed electrode arrays. The feasibility of applying to sEMG decomposition is also verified, where the motor unit action potential trains (MUAPTs) for single hand gesture and continuous hand gestures can be decomposed under different levels of isometric contractions, respectively. In summary, the proposed integrated all 3D-pinted process can achieve fast and simplified manufacturing of customized soft high-density electrode arrays, which can realize accurate, stable, and continuous monitoring of sEMG signals and be applied to muscle group pathology research and sEMG decomposition.

2. Results

2.1. 3D Printing of Soft High-Density Electrode Arrays

The primary objective of our research is to simplify the manufacturing process of customized soft high-density sEMG electrode arrays to achieve integrated continuous multimaterial fabrication, eliminating any manual or cumbersome processes. Thus, we propose a novel all 3D-printed manufacturing method based

on the DIW 3D printing technique to enable integrated manufacturing. Owing to the unique properties of 3D printing, we design a four-layer stacked structure for the soft high-density electrode arrays which allows for the continuous printing of various components required for the electrode's functionality. To enable the seamless interfacial integration during the multimaterial printing, we extensively study the printability of inks with different viscoelasticity. Based on the results of quantification, we further select optimal printing parameters, and design rational printing patterns for each functional layer to realize programmable, continuous, streamlined fabrication of soft high-density sEMG electrode arrays.

2.1.1. Structure Design of Soft High-Density Electrode Arrays

The printing structures are constrained to process from the bottom to the top, which means the electrode arrays are preferred to be designed as a stacked structure. As depicted in Figure 1B, a soft high-density electrode array is presented with a four-layer stacked structure, including the base layer, the conductive electrode layer, the encapsulation layer, and the filling layer. We choose thePI film, soft and long-term stability, as the base to support the materials printed on the thin film. The circular electrodes are made of elastic Ag paste with a typical radius of 1.5 mm.[31] Besides, the number of electrodes up to 32 is arranged in a 4 × 8 rectangular pattern with 8 mm space. The polylines play the role of connecting each circular electrode and terminal pad, which commonly form the conductive layer. To address signal crosstalk and interference, an encapsulation layer, composed of Ecoflex 0030 silicone rubber, is printed on the conductive layer and the base layer with hollow structures to expose circular electrodes. The soft silicone rubber layer can enhance the stability of the electrode arrays and endow such arrays better conformability with the skin. To compensate for the height differences between the conductive layer and encapsulation layer, the Ag filling layer is printed on the exposed circular electrodes to make the conductive areas slightly higher than the encapsulation layer, which can ensure stable signal transmission between the skin-electrode interface.

2.1.2. Printability Evaluation of Multimaterials

Each layer of electrode arrays contains specific materials and structures that may be fabricated by combining various processes conventionally. To simplify and streamline the manufacturing process, we pursue a digital method that enables integrated manufacturing of these stacked electrode structures, where the DIW 3D printing technique is a promising method (Figure 1C).

Figure 2A illustrates the typical printing mechanism and parameters used in the DIW process. The viscoelastic ink is extruded out of the moving nozzle tip, with the inner diameter D, by air pressure P. The air pressure P and nozzle inner diameter D jointly determine the extrusion speed of printing inks V_e, and the speed of moving nozzle can be defined as V_p. The viscoelastic ink is deposited onto the substrate at a certain height H through the printing nozzle, resulting in a filament with a specific diameter d. Therefore, the filament diameter is mainly influenced by four main parameters: P, D, H, and V_p, which may lead to die-swelling, thinning, and discontinuous linetype.[32–34] However, to achieve full printing of the predesigned structure, some issues need to be addressed in advance. For example, it is crucial to achieve a suitable line width for the conductive layer, which ensures proper electrical impedance and a compact arrangement for 32 channels. On the other hand, printing miniature hollow structures of the encapsulation layer with relatively low viscoelasticity ink can induce low shape fidelity, compared to the elastic Ag ink (Figure 2B). To accurately print a multi-hole encapsulation layer that seamlessly aligns with the conductive layer, it is essential to carefully evaluate the printability of multimaterials.

Hence, we first study the relationship between the diameter of printed filaments and printing parameters to investigate the printability of the chosen materials including elastic Ag ink and Ecoflex 0030 ink. Given that all the four parameters mentioned previously can affect the diameter of the printed filaments, we aim to reduce the variables and investigate the impact of the main factors on the lineshape during the printing process. Therefore, the diameter of filaments printed with different pressures P and printing speeds V_p are studied with constant printing height H and nozzle inner diameter D. For the elastic Ag ink, we maintain a printing height of 0.1 mm and use a 0.16 mm (30 Ga) nozzle, while vary the printing speed at 0.5, 1, 2, 3, 4, 5, 6, 7, 8, and 9 mm s^{-1}. For the Ecoflex 0030 silicone rubber ink, a printing height of 0.3 and a 0.26 mm (25 Ga) nozzle are applied, with the same varying printing speeds depicted before. Each experimental condition is printed in 4 trials under three different air pressures: 100, 200, and 300 kPa. The diameter of each filament is observed and measured using an electron microscope (detailed optical images of printed filaments are shown in Figure S1, Supporting Information). The results, as shown in Figure 2C, display the printability of Ag ink and Ecoflex 0030 at different printing parameters, which are divided by the fracture of filament and distortion rate. To further quantify the data, detailed statistics of poor shape fidelity and printable parameters are plotted for Ag ink and Ecoflex 0030 ink, respectively (Figure 2D and E). The whole changing tendency (plotted as the dashed curves) can be obtained through the following exponential function as:

$$d = \lambda_1 \cdot e^{\lambda_2 \cdot V_p} + \lambda_3 \cdot e^{\lambda_4 \cdot V_p} \quad (1)$$

where the $\lambda_{i=1,2,3,4}$ denote four varied fitting parameters. It's shown that the filament diameters decrease with the increase of printing speed at the same air pressure. Moreover, at the same printing speed, the filament diameters exhibit a positive correlation with the applied air pressure, which is consistent with the observations from other printing studies.[34] It is worth noting that discontinuous filaments occur under specific conditions, such as 100 kPa and 4 mm s^{-1} for the Ag ink, and 100 kPa and 7 mm s^{-1} for the Ecoflex 0030 ink. Additionally, the measured experimental values are all larger than the diameter of the printing nozzles, indicating that higher printing speeds may be required to achieve filament widths smaller than the nozzle diameter. Subsequently, we further explore the relationship between printing layer height h and printing speed V_p under different air pressures (200, and 300 kPa) for characterizing printing parameters of the filling layer, which shows similar inverse exponential curves (Figure S2, Supporting Information).

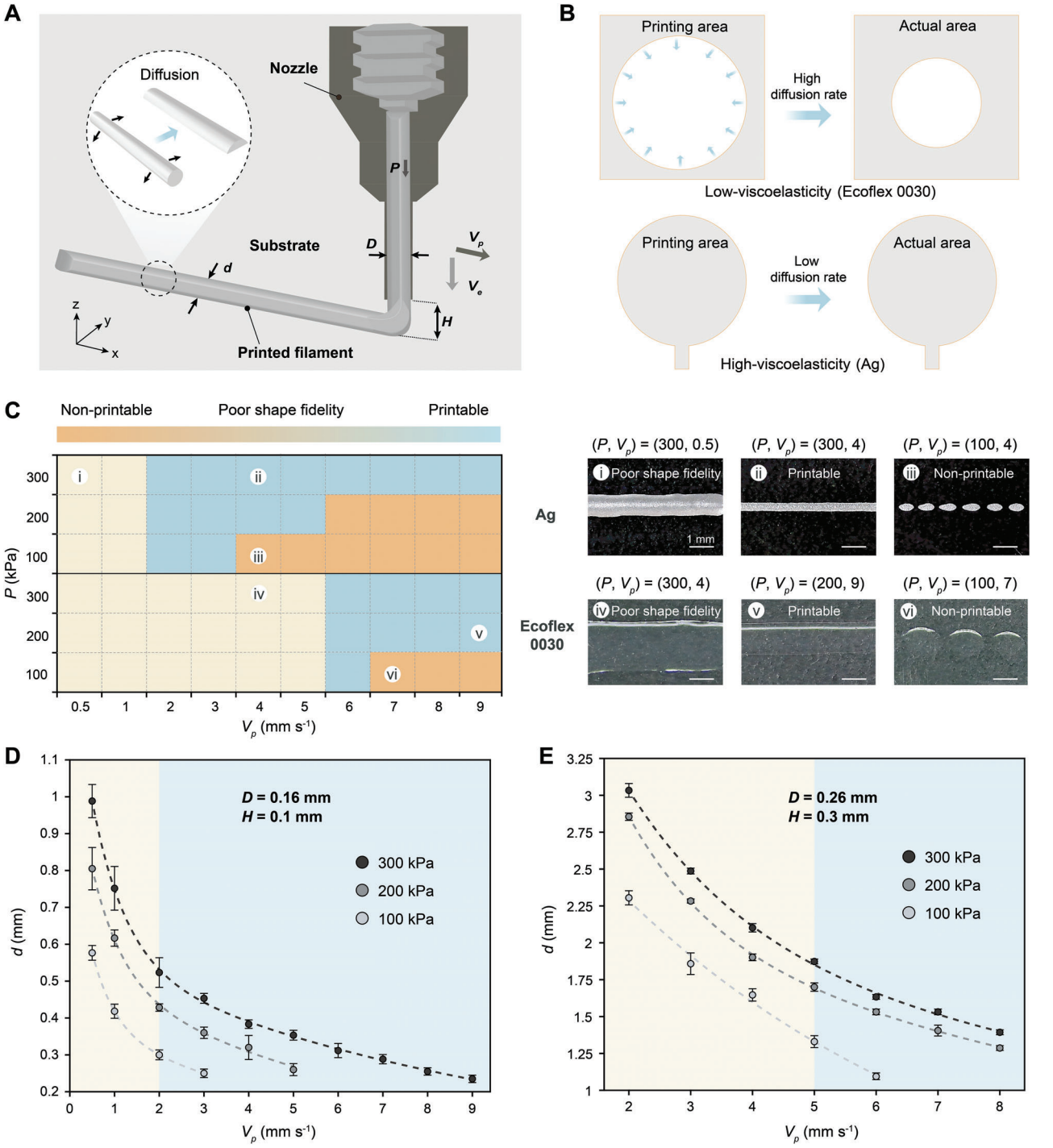

Figure 2. Printability evaluation of multimaterial inks. A) Schematic illustration of the DIW 3D printing. The filaments are extruded out of the moving nozzle by air pressure, which may diffuse depending on the viscoelasticity of the inks. B) The phenomenon of printing two types of inks with significant differences in viscoelasticity. For low-viscoelastic inks such as Ecoflex 0030, the accuracy of the printed structure will reduce significantly due to the diffusion effect. In contrast, high-viscoelastic ink (Ag ink) can maintain a high printing fidelity. C) Phase diagram shows the printability of Ag ink and Ecoflex 0030 ink at different printing parameters. Based on the fracture of filaments and distortion of diameter, the area of printability for two materials is distinguished into three colors: orange, yellow, and blue. when the applied pressure is far above the critical value or the printing speed is too slow, dramatic die welling occurs, leading to a low-resolution printing. On the contrary, low air pressure and high printing speed may cause the fracture. The i–vi) labels on the figure refer to the typical printing condition. Scale bars, 1 mm. D) The relationship between the diameter of Ag filaments and the printing speed under different pressures (100, 200, and 300 kPa). The printing height is set as 0.1 mm with the 0.16 mm nozzle. E) The relationship between the diameter of Ecoflex 0030 filaments and the printing speed under different pressures (100, 200, and 300 kPa). The printing height is set as 0.3 mm with the 0.26 mm nozzle. Data in D and E) are means ± standard deviation (SD), n = 4.

2.1.3. Printing Pattern Design and Manufacturing

Based on systematic ink printability evaluation, optimal printing parameters are meticulously selected to achieve high printing fidelity, and accordingly rational printing patterns are designed to realize seamless interfacial integration during the multimaterial printing. For the conductive electrode layer, we aim to make a balance between low impedance and compact line routing, choosing a printing pressure of 300 kPa and a speed of 3 mm s^{-1}. On the other hand, for the encapsulation layer, 200 kPa pressure and 6 mm s^{-1} printing speed are selected to ensure fast manufacturing while maintaining sufficient printing accuracy to create the required hollow structures in the millimeter range. Lastly, for the filling structure, we opt for a lower printing speed of 2 mm s^{-1} and 300 kPa pressure, which ensures the printing parameters in the printable area and the elastic Ag ink can be stacked effectively to construct a convex, well-formed filling layer slightly higher than the encapsulation layer.

After selecting appropriate printing parameters, the printing patterns, composed of coherent lines, are designed for each functional layer by taking into account the chosen parameters and the electrode structures. For the conductive layer, the circular electrodes are formed through the splicing of concentric arcs, of which the distance is defined as 0.3 mm less than the diameter of printed filaments (Figure S3, Supporting Information). Similarly, the line distance is set as 0.8 mm less than the diameter of filaments for the encapsulation layer, which allows for rapid printing and forming of flat planes. We expand the dimension of the hollow structures larger than the size of circular electrodes to eliminate the influence of diffusion effects (Figure S4, Supporting Information). For the filling layer, we choose the concentric arcs with higher density (distance, 0.15 mm) to achieve the convex structure of electrodes (Figure S5, Supporting Information).

Based on the predesigned printing patterns, the electrode arrays are manufactured through the proposed all-printed strategy by our customized DIW printer as shown in Figure 1C and **Figure** 3A. We pick one yellow or transparent PI film (thickness, 0.25 mm) with a size of 80 × 80 mm undergoing plasma cleaning to enhance the hydrophilicity of the base layer and adhesion ability for materials (Figure S6, Supporting Information). Subsequently, the proposed all 3D printing process is divided into three continuous steps. First, the PI film is moved to the printing platform to print the conductive layer with the Ag ink and the corresponding printing nozzle (0.16 mm). Then the printing ink is switched to Ecoflex 0030 to print the encapsulation layer with 0.26 mm printing nozzle. Once the encapsulation layer is completed, the printing ink and nozzle are replaced again to print the electrode filling layer (Movie S1, Supporting Information). Noted that due to the rapid curing or volatilization characteristics of printing inks and hundreds of micrometers printing height, post-process conditions of printing patterns for all functional layers just need to be set as 25 °C in 10 min between each manufacturing step, which can lead to a reproducible, continuous, streamlined fabrication for high-density multi-channel electrode arrays (Figure 3B). The structural stability of the printing electrode array is also validated by cyclic bending test. The results show that the all-printed high-density electrode arrays possess robust structural stability even after 1000 bending cycles (Figure S7, Supporting Information). Moreover, we design and fabricate a 32-channel irregular spindle shaped electrode array based the same process to demonstrate the capability of customized manufacturing (Figure S8, Supporting Information).

2.2. Electrode Evaluation and Validation

After manufacturing in the proposed all 3D-printed process, we conduct a comprehensive evaluation to assess the performance and feasibility of the soft high-density electrode arrays, including varying electrical characterizations, muscle activation mapping test, and sEMG decomposition verification.

2.2.1. Electrical Characterization

As one of the main factors affecting the quality of recorded sEMG signals, the impedance of the skin-electrode interface is measured by the electrochemical impedance spectroscopy (EIS) test. To compare the impedance of electrodes, two types of electrodes (Ag/AgCl electrodes and size-matched printed electrodes) are tested on the same skin position of the forearm by a standard three-electrode method. And the representative recorded data is plotted as the bode diagram including impedance moduli and phase of the skin-electrode interface (Figure 3C and D). The results show that these two electrodes possess similar curves of impedance moduli in the low-frequency field, such as the field of 10^5 Ω. A similar phenomenon is also observed in the phase spectrum with the extreme value appearing near 1000 Hz. To further eliminate the influence of impedance on electrode sizes, we compare the 10 Hz (the low-frequency region of sEMG signals) cutaneous impedance modulus, normalized by the electrode geometric surface area (GSA) (Figure 3E). The average GSA-normalized skin impedance of the printed electrodes is 2.6×10^5 Ω cm^2, which is slightly lower than that of the Ag/AgCl electrodes. It is worth noting that the impedance of printed electrodes is measured without using any conductive gels or creams, which are critical for the compared electrodes to achieve equitable skin-electrode impedances. Meanwhile, the skin-electrode impedance of our 32-channel electrode array is also characterized and remains consistent similar to the printed single electrode (Figure S9, Supporting Information).

Furthermore, we wonder if a relatively low skin-electrode impedance can lead to a better performance of monitoring sEMG signals. A SNR test is conducted to verify the recording capability of high-density electrode arrays by acquiring sEMG signals from the forearm muscles of five healthy human subjects. To reduce the impact of individual differences on strength, the MVC force of each subject is calibrated using a force dynamometer as shown in Figure 3F. Three different types of electrodes, including printed high-density electrode arrays, commercial high-density electrode arrays (OT64, GR04MM1305, OT Bioelettronica), and Ag/AgCl electrodes, are used to compare the quality of recorded sEMG signals. In the experiments, the subjects are instructed to perform isometric contraction of grasp to follow the guideline

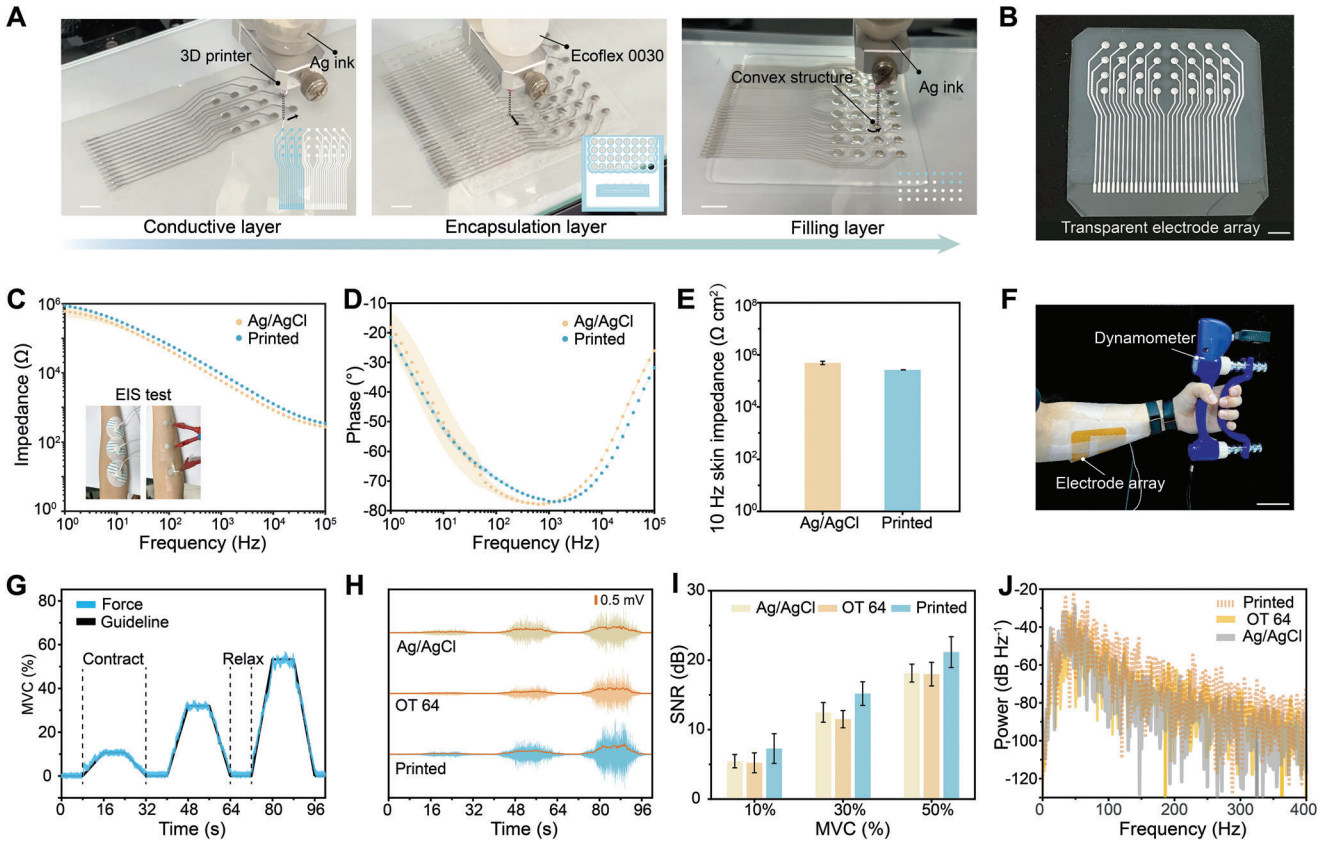

Figure 3. 3D printing of soft high-density sEMG electrode arrays and their electrical performance. A) Sequential snapshots for 3D printing of the layer-stacked high-density electrode arrays by two different viscoelastic inks. B) Image of the transparent 32-channel printed electrode array. C) Comparison of bode diagram of the impedance moduli between our printed electrodes and Ag/AgCl electrodes by EIS test based on the standard three-electrode method. D) Comparison of bode diagram of the phase between our printed electrodes and Ag/AgCl electrodes. E) Comparison of GSA-normalized 10 Hz cutaneous impedance modulus of our printed electrodes with Ag/AgCl electrodes. Data are plotted as means ± SD, n = 3. F) Image of the experimental setup of isometric contractions with the yellow high-density electrode array pasted on the forearm. G) Experimental paradigm of the isometric contraction and sEMG monitoring. Isometric contractions of 10%, 30%, and 50% MVC force levels are done in sequence under the guideline (black solid line), and the blue curve represents the actual exerted force of one representative subject. H) Comparison of sEMG amplitudes of different electrodes recorded from the same position. The orange curves represent the RMS envelope of each sEMG signal. I) Comparison of representative SNR results of the recruited subject for different electrodes under isometric contractions. Data are plotted as means ± SD, n = 3. J) Comparison of the power spectral density of the recorded sEMG signals for different electrodes. The curves of OT 64 and Ag/AgCl electrode overlap throughout the frequency domain, and printed high-density electrode array performs better. Scale bars, 10 mm A); 10 mm B); 5 cm F); 0.5 mV H).

of forces at 10%, 30%, and 50% of their MVC for three trials (Figure 3G). Each contraction task comprises three phases: steady rise, constant stage, and steady decline, with each phase lasting for 8 s. To avoid muscle fatigue, an interval of 8 s is set to allow subjects to have enough rest time. sEMG signals of activation are recorded with the corresponding force data simultaneously.

To quantify the recording performance, we select the signals collected from the same position of the skin for comparison. The data is notch-filtered offline at 50 Hz to eliminate power frequency noise, followed by bandpass filtering between 10–400 Hz. The root-mean-square (RMS) envelope of the filtered signal is calculated using a 200 ms wide moving window, with 100 ms overlap. Representative results of recorded sEMG signals from one subject are shown in Figure 3H for each type of electrodes. It is noted that the signal amplitude of the printed electrode arrays is significantly higher than that of the OT 64 electrode arrays and the Ag/AgCl electrodes. For further quantification of the quality of sEMG signals, the SNR value is calculated by using the middle 4 s data of each contraction level. The average SNR of each subject for different contraction levels is computed as follows:

$$SNR_{MVC} = \frac{\sum_{n=1}^{3}\sum_{i=1}^{40} 20 \cdot \log_{10}\left(\frac{RMS_n^i}{RMSR_n}\right)}{n \cdot i} \quad (2)$$

where RMS_n^i denotes the RMS value of the number i moving window of experimental trial n in constant stage, and the $RMSR_n$ denotes the first middle 2 s rest RMS value of experimental trial n. The SNR_{MVC} is the general SNR value under different MVC levels including 10%, 30%, and 50%, which is calculated by averaging the SNR value of all moving windows.

The calculated data for all individuals are plotted as the columnar bar in the supporting information (Figure S10, Supporting Information). A representative SNR result of the subject is shown in Figure 3I. It is indicated that the printed electrode arrays have

an average SNR of 15.2 ± 1.7 dB with a 32.2% enhancement compared to the commercial high-density electrode arrays (11.5 ± 1.2 dB) under 30% MVC, which is also higher than the Ag/AgCl electrodes (12.5 ± 1.4 dB). Subsequently, we transform the time domain of raw sEMG signals into the frequency domain to compare the quality of signals. The power spectral density of the 30% MVC sEMG signals is depicted in Figure 3J, indicating that the printed electrode arrays outperform the counterparts across the entire spectrum. In general, the printed electrode arrays are more sensitive in recording sEMG signals compared to the other electrodes, whether in the time domain characteristics or frequency domain characteristics. The improvement in signal quality is partly due to the relatively low impedance characteristics of the conductive Ag ink used in the printed electrode arrays. Meanwhile, the convex structure and the soft silicone rubber material enable the electrode arrays can maintain a good connection to the skin without using conductive creams, further enhancing the capability of recording electrophysiological signals.

2.2.2. Spatial Mapping of Muscle Activation

In this section, we further demonstrate the capability of joint acquisition of printed high-density electrode arrays, which is also referred to as the spatial resolution, based on the 4×8 arrangement arrays. It is generally true that the highly sensitive surface electrodes can significantly improve diagnosability in muscle cartography studies,[35–38] where the muscle activation blocks can be monitored and tracked. Thus, we recruit the participants to do the muscle activation mapping test by pasting the high-density electrode arrays on the FDS muscle of the forearm. During the experiments (Movie S2, Supporting Information), subjects are informed to do four different hand gestures, which are all associated with muscle groups of FDS including index finger pinch, middle finger pinch, ring finger pinch, and little finger pinch. Each gesture needs to be held for 5 s with subjectively stable and large force, then continuously transferred one by one with the 5 s interval of rest. Three trials are performed with a computer timer to guide subjects to execute the entire experiment, and sEMG data are collected simultaneously.

In order to visualize the patterns of muscle activation accompanied with hand gestures, heat maps are constructed based on the RMS values of the sEMG signals obtained from the 4 × 8 electrode array. Note that the heat maps are interpolated linearly to implement a smooth coupling of different electrode areas. The values of the color bars, representing the range of RMS, vary depending on the applied power and the performed hand gesture. The contraction centroids of the RMS values are highlighted in yellow, where darker areas indicate lower muscle activation. **Figure** 4A displays three representative RMS heat maps with 1 s interval for index finger pinch (the heat maps for other gestures are shown in Figure S11, Supporting Information). The result shows that the contraction centroid of muscle activation is located at the bottom left of the electrode array initially. Although some fluctuations occur during the activation process, the overall trend remains almost consistent. When different fingers are pinched separately, the RMS heat maps of the first second of each gesture map out the distinct activation regions of FDS muscle groups as shown in Figure 4B. The centroids of activation shift from the bottom left corner of the electrode array to the top right gradually, which is consistent with the distribution of the groups of FDS muscle in anatomy.[37] The obtained results demonstrate that the printed high-density electrode arrays can provide spatiotemporal maps depicting the activation of muscle groups, which also confirm the capability of joint acquisition and high spatiotemporal resolution.

2.2.3. Verification of High-Density sEMG Decomposition

The high-density electrode array as the recording tool for sEMG decomposition research is necessary to verify the feasibility of decomposing the credible motor units (MUs) based on the mature myoelectric decomposition algorithm.[39,40] In this section, we first scheme an experiment to validate that the arrayed sEMG signals recorded from the printed electrode arrays can decompose corresponding MUAPTs from single hand gesture. Then another experiment is further implemented for the continuous decomposition of multiple hand gestures.

The sEMG data are recorded from the FDS of the forearm, using the same method mentioned before. The collected data are analyzed by the decomposition algorithm proposed in our previous work.[41–43] A representative example of MUAPTs decomposition for the gesture of four-finger grasp is shown in **Figure** 5A. 10 MUs are decoded from 32-channel sEMG signals, and each motor unit (MU) is represented by a different color. The discharge timings of different MUs are expressed by color bars. Meanwhile, synchronous force data, recorded by the dynamometer, are plotted as the gray shadow. It is noted that the behavior of MUs is closely related to the force of isometric contractions. There is a positive correlation between the number of recruited MUs and the intensity of the force. For the discharging training MU 9 and MU 10, these two MUs suddenly appear at the end of peak force, which might indicate that the subject intends to maintain a relatively slow force decline to stimulate additional MUs work. To indicate the waveforms of each MU, the maximum amplitudes of action potential are plotted alongside the spike trains respectively. The multi-channel action potentials are also extracted to illustrate the spatial distribution of each MU. To ensure the credibility of the decomposition, two unstable channel signals influenced by the motion artifact are removed during the offline algorithm, which results in the minor missing of the waveform distribution maps. Two representative MUs are shown in Figure 5B and Figure 5C. The results show that MU 9 is located at the lower left corner of the electrode array, and MU 6 presents an opposite waveform which is located on the right side.

Furthermore, we conduct the decomposition for the continuous and multiple hand gestures (Figure 5D). Two channels of sEMG signals are plotted, which are recorded during the hand gestures task including fist grasp, four-finger grasp, and three-finger grasp. It is shown that the signals of the same channel for different gestures correspond to different amplitudes and waveforms. Similarly, there are significant waveform differences between these two channels for the same hand gesture, which also confirms the spatiotemporal characteristics of electrode arrays. Further, the offline decomposition results of continuous hand gestures are plotted with the force data labeled as the gray shadow. Various MUs are decomposed and the discharge features

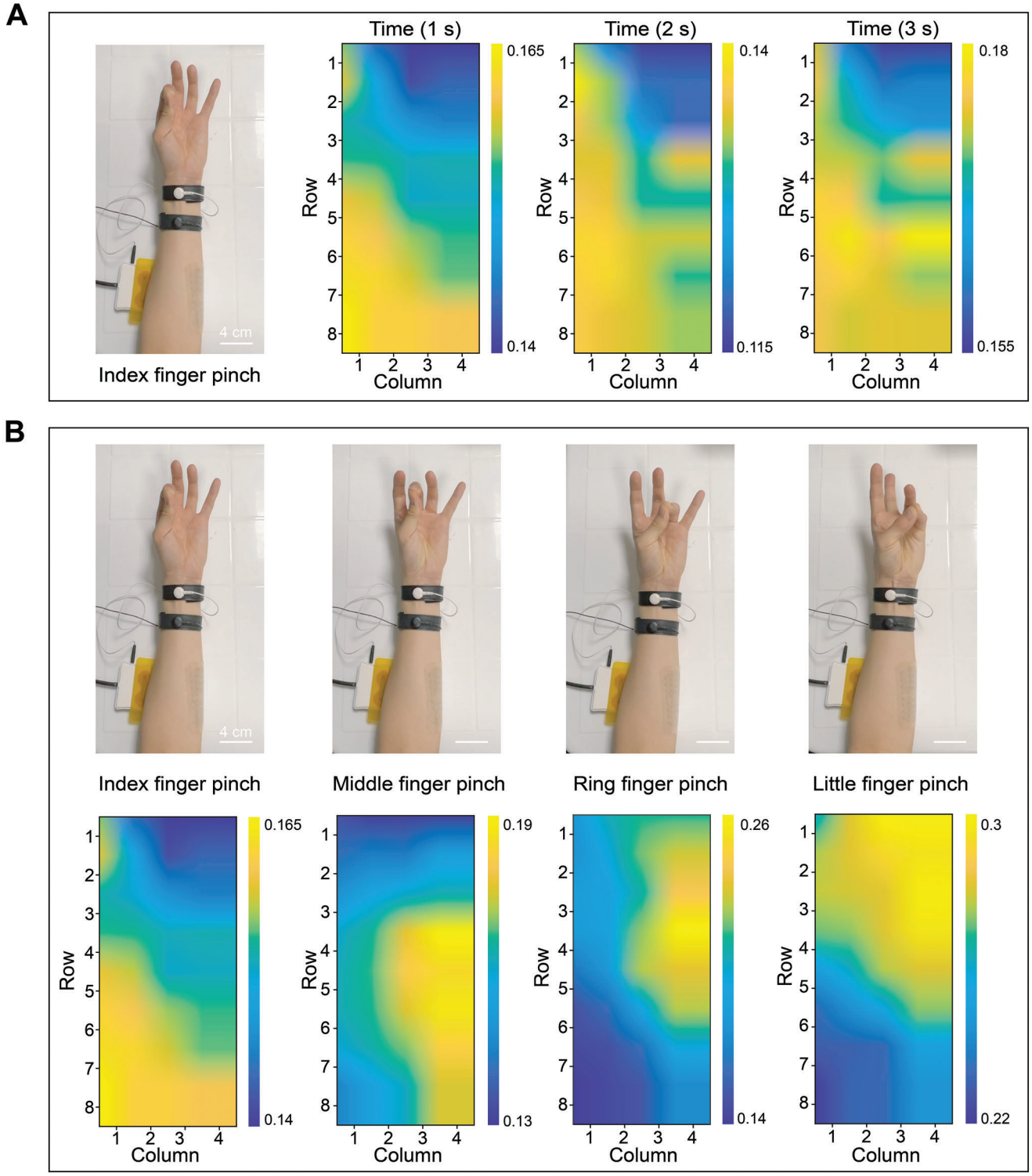

Figure 4. Spatial mapping of FDS muscle activation. A) Spatial variation of contraction centroids for index finger pinch with time changing. The heat maps are plotted by calculating the RMS values of 32-channel sEMG signals at different time. Due to the subjective control of the hand gesture, the values of the color bars change over time. B) Spatial variation of contraction centroids for continuous hand gestures. The heat maps represent the RMS values of each gesture in the first second. To make the results more prominent, linear interpolation processing is performed for all heat maps. Scale bar, 4 cm A,B).

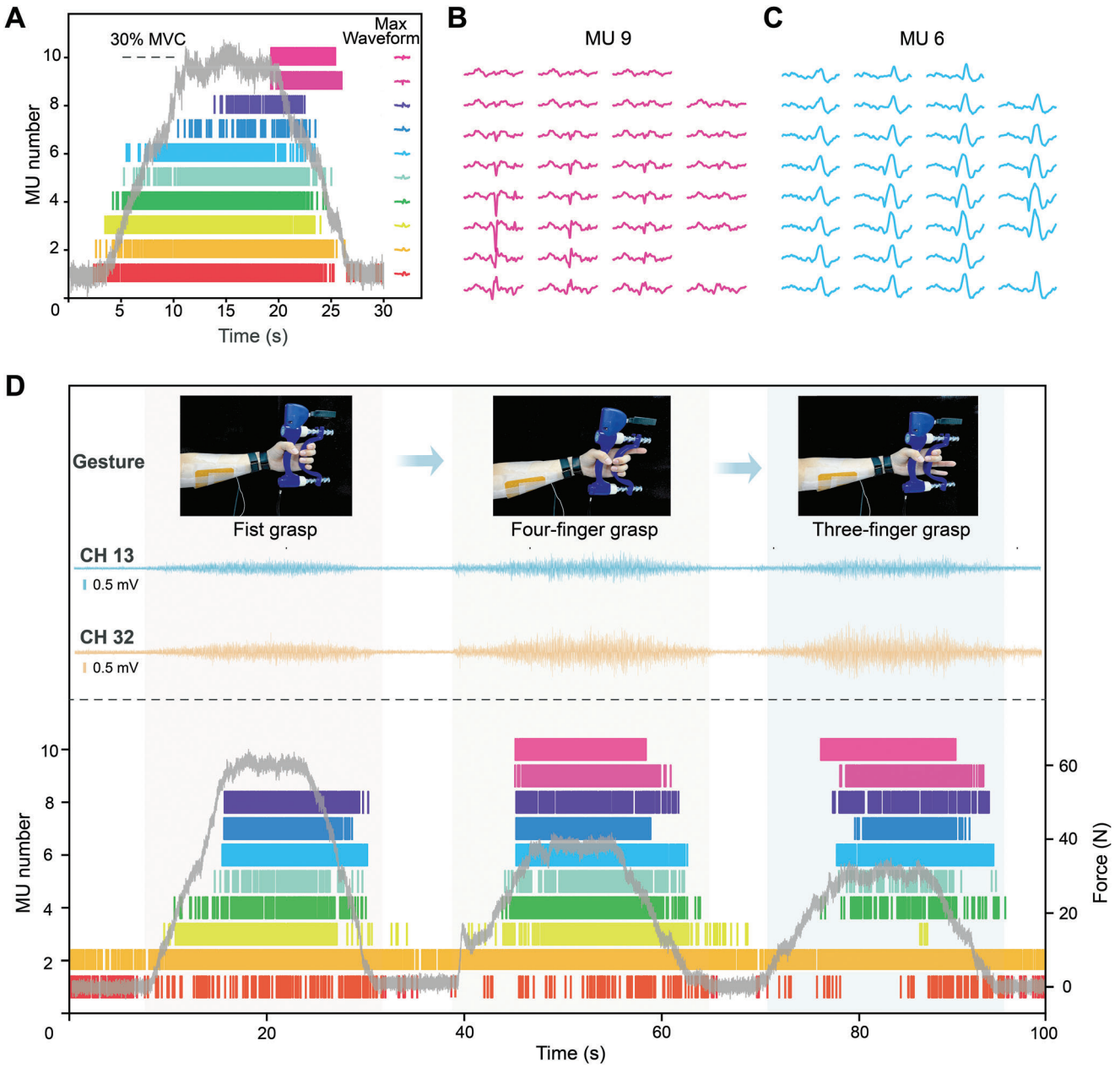

Figure 5. Verification of sEMG decomposition for all 3D-printed high-density electrode arrays. A) sEMG decomposition for single hand gesture. A representative decomposition result for four-finger grasp is plotted with the force curve. B) The motor unit action potential waveforms of MU 9. C) The motor unit action potential waveforms of MU 6. Due to changes in hand movements and force levels in the experiment, fluctuations occur in the collection of high-density sEMG signals. In order to ensure the credibility of the decomposition, two unstable channel signals are removed during the offline algorithm, which results in the missing of two positions in the last column of the waveform distribution maps of MU 9 and MU 6. D) Continuous sEMG decomposition for multiple hand gestures. Each color bar of the background demonstrates the decomposed MUAPTs and dual-channel sEMG signals are plotted for corresponding hand gestures. Scale bar, 0.5 mV.

of MUAPTs are consistent with the curve of force information. Among the MUs, some are recruited throughout the process, and some are just used for specific hand gestures. For instance, each grasp gesture contains the MU 8, yet MU 9 and MU 10 are only recruited during the four-finger grasp and three-finger grasp. Moreover, although MU 3 is recruited by all gestures, it plays a negligible role in the three-finger grasp. It is noted that MU 1 and MU 2 are almost recruited throughout the entire experimental process, whether in a rest or grasp state. This is due to the subjects need to hold the force dynamometer horizontally, resulting in a minor number of MUs discharging throughout the entire process, which also confirms the superior recording capability of our printed electrode arrays for weak sEMG signals. All these distinguishable information implied in the decomposed results can be used to identify specific hand gestures in later research.

In this section, two experiments are designed to verify the feasibility of applying the printed electrode arrays to sEMG decomposition research. The results show that the recorded sEMG signals of high-density electrode arrays can decompose enough MUs and corresponding MUAPTs. Compared to the existing commercial high-density electrodes, the proposed all-printed electrode arrays could modify the electrode alignment and patterns for various muscle groups to meet diverse requirements, which are promisingly applied to the innovative human-machine interface mode toward practical applications such as teleoperation and prosthetic control.

3. Conclusion

In this study, we demonstrate a novel all 3D-printed process to manufacture customized programmable, soft high-density sEMG electrode arrays by continuous multimaterial printing. Two inks with significant differences in viscoelasticity are characterized based on the DIW technique, and rational printing parameters are selected to eliminate the diffusion effect to achieve high fidelity printing. Meanwhile, optimal printing patterns are designed and printed in sequence to achieve seamless manufacturing of high-performance 32-channel sEMG electrode arrays. A comprehensive evaluation is conducted to assess the performance and feasibility of the soft high-density electrode arrays, including electrical characterization, spatial resolution test, and signal decomposition verification. The results show that the printed electrode arrays exhibit a low skin-electrode impedance and a significant enhancement in signal quality. Furthermore, the efficacy of electrode arrays is also validated by applying to accurate muscle activation mapping and sEMG signal decomposition. To achieve the higher electrode array density under the same patch area, a multi-layer interconnection conductive path based on all 3D-printed method can be developed in future research by structure-transition to multidimensional arrays. Overall, the proposed all 3D-printed technique not only addresses the existing challenges in integrated multimaterial 3D printing, but also provides a promising platform to achieve simplified and customized manufacturing of high-performance electrode arrays for diverse applications like flexible electronics, wearable devices, and bioelectronics.

4. Experimental Section

Preparation of 3D Printable Inks: The ink of Ecoflex 0030 (Smooth-On) was prepared by mixing equivalent amounts of Parts A (10 g) and Parts B (10 g) for 3 min. Then pour the mixture into the customized 3D printer, which was equipped with the negative pressure function to achieve degassing. The Ecoflex 0030 ink could be printed in the following 45 min before self-curing. The Ag ink (BASE-SCD2, Prtronic) was a kind of stretchable conductive silver paste that had the ability to print on various substrates.

Curing Conditions: The conductive layer printed by elastic Ag ink was cured for 10 min at the room temperature (25 °C) to allow the ink solvent to fully evaporate. For the Ecoflex 0030 ink, the thin printed layer (thickness, 100 µm) results in fast cross-linking within a short time. Hence, the curing conditions for all functional layers were set as 25 °C in 10 min between each step in the entire all-printing process.

EIS Test: Three healthy subjects were recruited to do the impedance test. The skin of the forearm of each subject was cleaned with an alcohol pad. Then, three electrodes as the reference electrode, the counter electrode, and the working electrode were placed on the forearm equidistantly by adhesive tapes. And the EIS data were measured by the electrochemical workstation (AUTOLAB) with a frequency range of 1–10^5 Hz. 10 mV (peak-to-peak amplitude) sinusoidal signals were applied for all EIS measurements.

Monitoring of sEMG Signals: For the sEMG monitoring test, five adult subjects (4 males, 1 female, 23–31 years old) were recruited and consented to follow an approved protocol from the Institutional Review Board at Shanghai Jiao Tong University (SR2021-001). Subjects have no prior history of neuromuscular disorder, neuropathy, or myopathy, according to self-report. To account for variations in individual strength and the level of force exerted, the MVC force of each subject is calibrated using a force dynamometer (Biometrics Ltd). Three different types of electrodes were mounted above FDS muscle groups after the skin was cleaned using an alcohol pad. Additionally, two moist fabric straps were worn on the wrist to serve as the reference electrode and the ground electrode. All these electrodes were connected to a multi-channel amplifier (Quattrocento, OT Bioelettronica) with a gain of 500 and a sampling frequency of 2048 Hz. For the printed high-density electrode arrays, a customized transfer flexible printed circuit (FPC) was designed to connect between the electrode arrays and amplifier (Figure S12, Supporting Information). The terminal pads of electrode arrays were aligned and stuck with the transfer FPC adopting the anisotropic conductive film (3 M, 7303).

sEMG Decomposition: The decomposition experiment for single hand gesture was set up as follows: the recruited subjects were instructed to sit on the chair and place their hands horizontally in mid-air. The force dynamometer (Biometrics Ltd) was placed in the palm of their hand to measure the applied force. The printed high-density electrode arrays were then mounted on the muscle groups of the FDS after the cleaning treatment of the skin. The subjects were instructed to perform a hand gesture known as the four-finger pinch, simultaneously exerting a 30% MVC force. A trapezoidal force curve with 3 s rest before and after each contraction was set to guide the participants, and three trials were conducted. The verification experiment for continuous hand gestures adopted the same paradigm as described above, and three different hand gestures associated with the muscle groups of the FDS were conducted continuously with 8 s intervals under corresponding 30% MVC force. Each test was also conducted for three trials with sEMG signals and force information recorded simultaneously.

Statistical Analysis: All the results in this study were presented as mean ± SD, and all the mechanical properties presented in this study were measured from at least three parallel samples. Data distribution was assumed to be normal for all the parametric tests, but not formally tested, and no significant difference analysis was performed. The statistical analyses were carried out with the MATLAB R2020a software.

Supporting Information

Supporting Information is available from the Wiley Online Library or from the author.

Acknowledgements

This study was supported in part by the National Natural Science Foundation of China (Grant Nos. 52025057, 52227808 and 91948302), the Science and Technology Commission of Shanghai Municipality (Grant No. 22511101700).

Conflict of Interest

The authors declare no conflict of interest.

Data Availability Statement

The data that support the findings of this study are available from the corresponding author upon reasonable request.

Keywords

3D printing, decomposition, high-density electrode arrays, muscle activation mapping, sEMG monitoring

Received: October 10, 2023
Revised: December 6, 2023
Published online: December 22, 2023

[1] X. Navarro, T. B. Krueger, N. Lago, S. Micera, T. Stieglitz, P. Dario, *J. Peripher. Nerv. Syst.* **2005**, *10*, 229.
[2] C. Xie, Q. Yang, Y. Huang, S. Su, T. Xu, R. Song, *IEEE Trans. Biomed. Circuits. Syst.* **2021**, *15*, 1332.
[3] T. Teramae, T. Noda, J. Morimoto, *IEEE Robot. Autom. Lett.* **2018**, *3*, 210.
[4] G. Gu, N. Zhang, H. Xu, S. Lin, Y. Yu, G. Chai, L. Ge, H. Yang, Q. Shao, X. Sheng, X. Zhu, X. Zhao, *Nat. Biomed. Eng.* **2023**, *7*, 589.
[5] M. Laffranchi, N. Boccardo, S. Traverso, L. Lombardi, M. Canepa, A. Lince, M. Semprini, J. A. Saglia, A. Naceri, R. Sacchetti, E. Gruppioni, L. De Michieli, *Sci. Robot.* **2020**, *5*, 467.
[6] G. Gu, N. Zhang, C. Chen, H. Xu, X. Zhu, *ACS. Nano.* **2023**, *17*, 9661.
[7] M. J. Zwarts, D. F. Stegeman, *Muscle. Nerve.* **2003**, *28*, 1.
[8] G. Drost, D. F. Stegeman, B. G. M. Van Engelen, M. J. Zwarts, *J. Electromyogr. Kines.* **2006**, *16*, 586.
[9] Y. Luo, M. R. Abidian, J. H. Ahn, D. Akinwande, A. M. Andrews, M. Antonietti, Z. Bao, M. Berggren, C. A. Berkey, C. J. Bettinger, J. Chen, P. Chen, W. Cheng, X. Cheng, S. J. Choi, A. Chortos, C. Dagdeviren, R. H. Dauskardt, C. A. Di, M. D. Dickey, X. Duan, A. Facchetti, Z. Fan, Y. Fang, J. Feng, X. Feng, H. Gao, W. Gao, X. Gong, C. F. Guo, et al., *ACS Nano* **2023**, *17*, 5211.
[10] H. Wu, G. Yang, K. Zhu, S. Liu, W. Guo, Z. Jiang, Z. Li, *Adv. Sci.* **2021**, *8*, 2001938.
[11] S. M. A. Iqbal, I. Mahgoub, E. Du, M. A. Leavitt, W. Asghar, *Npj. Flex Electron.* **2021**, *5*, 9.
[12] S. Liu, Y. Rao, H. Jang, P. Tan, N. Lu, *Matter* **2022**, *5*, 1104.
[13] Y. Jiang, Z. Zhang, Y. Wang, D. Li, C. Coen, E. Hwaun, G. Chen, H. Wu, D. Zhong, S. Niu, W. Wang, A. Saberi, J. Lai, Y. Wu, Y. Wang, A. A. Trotsyuk, K. Y. Loh, C. Shih, W. Xu, K. Liang, K. Zhang, Y. Bai, G. Gurusankar, W. Hu, W. Jia, Z. Cheng, R. H. Dauskardt, G. C. Gurtner, J. B. Tok, K Deisseroth, et al., *Science* **2022**, *375*, 1411.
[14] F. Ershad, M. Houston, S. Patel, L. Contreras, B. Koirala, Y. Lu, Z. Rao, Y. Liu, N. Dias, A. Haces-Garcia, W. Zhu, Y. Zhang, C. Yu, *PNAS. Nexus.* **2023**, *2*, 291.
[15] L. Pan, H. Wang, P. Huang, X. Wu, Z. Tang, Y. Jiang, S. Ji, J. Cao, B. Ji, G. Li, D. Li, Z. Wang, X. Chen, *Adv. Mater.* **2023**, *35*, 2301290.
[16] M. Reis Carneiro, C. Majidi, M. Tavakoli, *Adv. Funct. Mater.* **2022**, *32*, 2205956.
[17] S. Velasco-Bosom, N. Karam, A. Carnicer-Lombarte, J. Gurke, N. Casado, L. C. Tomé, D. Mecerreyes, G. G. Malliaras, *Adv. Healthcare Mater.* **2021**, *10*, 2100374.
[18] A. Moin, A. Zhou, A. Rahimi, A. Menon, S. Benatti, G. Alexandrov, S. Tamakloe, J. Ting, N. Yamamoto, Y. Khan, F. Burghardt, L. Benini, A. C. Arias, J. M. Rabaey, *Nat. Electron.* **2020**, *4*, 54.
[19] Y. Yu, J. Li, S. A. Solomon, J. Min, J. Tu, W. Guo, C. Xu, Y. Song, W. Gao, *Sci. Robot.* **2022**, *7*, 495.
[20] B. B. Murphy, P. J. Mulcahey, N. Driscoll, A. G. Richardson, G. T. Robbins, N. V. Apollo, K. Maleski, T. H. Lucas, Y. Gogotsi, T. Dillingham, F. Vitale, *Adv. Mater. Technol.* **2020**, *5*, 2000325.
[21] P. Fayyaz Shahandashti, H. Pourkheyrollah, A. Jahanshahi, H. Ghafoorifard, *Sensor. Actuat. A-Phys.* **2019**, *295*, 678.
[22] B. W. Stuart, X. Tao, D. Gregory, H. E. Assender, *Appl. Surf. Sci.* **2020**, *505*, 144294.
[23] N. Driscoll, B. Erickson, B. B. Murphy, A. G. Richardson, G. Robbins, N. V. Apollo, G. Mentzelopoulos, T. Mathis, K. Hantanasirisakul, P. Bagga, S. E. Gullbrand, M. Sergison, R. Reddy, J. A. Wolf, H. I. Chen, T. H. Lucas, T. R. Dillingham, K. A. Davis, Y. Gogotsi, J. D. Medaglia, F. Vitale, *Sci. Transl. Med.* **2021**, *13*, 8629.
[24] R. Garg, N. Driscoll, S. Shankar, T. Hullfish, E. Anselmino, F. Iberite, S. Averbeck, M. Rana, S. Micera, J. R. Baxter, F. Vitale, *Small Methods* **2023**, *7*, 2201318.
[25] H. Lee, S. Lee, J. Kim, H. Jung, K. J. Yoon, S. Gandla, H. Park, S. Kim, *Npj. Flex. Electron.* **2023**, *7*, 20.
[26] S. Chandra, J. Li, B. Afsharipour, A. F. Cardona, N. L. Suresh, L. Tian, Y. Deng, Y. Zhong, Z. Xie, H. Shen, Y. Huang, J. A. Rogers, W. Z. Rymer, *IEEE T. Bio-Med. Eng.* **2021**, *68*, 1389.
[27] H. Yuk, B. Lu, S. Lin, K. Qu, J. Xu, J. Luo, X. Zhao, *Nat. Commun.* **2020**, *11*, 1604.
[28] R. L. Truby, J. A. Lewis, *Nature* **2016**, *540*, 371.
[29] J. Li, J. Cao, B. Lu, G. Gu, *Nat. Rev. Mater.* **2023**, *8*, 604.
[30] D. Wang, J. Wang, Z. Shen, C. Jiang, J. Zou, L. Dong, N. X. Fang, G. Gu, *Annu. Rev. Contr. Robot.* **2023**, *6*, 31.
[31] B. Afsharipour, S. Soedirdjo, R. Merletti, *Biomed. Signal. Process* **2019**, *49*, 298.
[32] H. Yuk, X. Zhao, *Adv. Mater.* **2018**, *30*, 1704028.
[33] G. Chen, X. Liang, P. Zhang, S. Lin, C. Cai, Z. Yu, J. Liu, *Adv. Funct. Mater.* **2022**, *32*, 2113262.
[34] X. Peng, S. Wu, X. Sun, L. Yue, S. M. Montgomery, F. Demoly, K. Zhou, R. R. Zhao, H. J. Qi, *Adv. Mater.* **2022**, *34*, 2204890.
[35] A. Radmand, E. Scheme, K. Englehart, *J. Rehabil. Res. Dev.* **2016**, *53*, 443.
[36] X. Hu, N. L. Suresh, C. Xue, W. Z. Rymer, *Front. Physiol.* **2015**, *6*, 279.
[37] L. Meng, Q. Chen, X. Jiang, X. Liu, J. Fan, C. Dai, W. Chen, *Biomed. Signal. Proces.* **2022**, *75*, 103615.
[38] C. Dai, X. Hu, *Int. J. Neural. Syst.* **2019**, *29*, 1850025.
[39] D. Farina, N. Jiang, H. Rehbaum, A. Holobar, B. Graimann, H. Dietl, O. C. Aszmann, *IEEE T. Neur. Sys. Reh.* **2014**, *22*, 797.
[40] D. Farina, I. Vujaklija, M. Sartori, T. Kapelner, F. Negro, N. Jiang, K. Bergmeister, A. Andalib, J. Principe, O. C. Aszmann, *Nat. Biomed. Eng.* **2017**, *1*, 25.
[41] C. Chen, S. Ma, X. Sheng, D. Farina, X. Zhu, *IEEE Trans. Biomed. Eng.* **2020**, *67*, 3501.
[42] E. Martinez-Valdes, C. M. Laine, D. Falla, F. Mayer, D. Farina, *Clin. Neurophysiol.* **2016**, *127*, 2534.
[43] C. Chen, Y. Yu, S. Ma, X. Sheng, C. Lin, D. Farina, X. Zhu, *Biomed. Signal. Proces.* **2020**, *55*, 101637.